RSC Advances

PAPER

View Article Online
View Journal | View Issue

Cite this: *RSC Adv.*, 2017, **7**, 15139

Effect of annealing atmosphere on quaternary chalcogenide-based counter electrodes in dye-sensitized solar cell performance: synthesis of Cu_2FeSnS_4 and Cu_2CdSnS_4 nanoparticles by thermal decomposition process†

Krishnaiah Mokurala* and Sudhanshu Mallick*

The synthesis of stoichiometrically controlled quaternary chalcogenide nanoparticles through a simple, eco-friendly process is still a great challenge. Herein, earth-abundant quaternary chalcogenide nanoparticles, Cu_2FeSnS_4 (CFTS) and Cu_2CdSnS_4 (CCdTS), were synthesized *via* the thermal decomposition of metal precursors. The prepared CFTS and CCdTS films were used as alternative counter electrodes (CEs) in dye-sensitized solar cells (DSSCs). The effects of the annealing atmosphere on morphology, elemental composition, electrical properties and electrochemical catalytic activity of the CFTS and CCdTS films were investigated. Energy dispersive spectroscopy, Hall measurements, cyclic voltammetry, and electrochemical impedance spectroscopy analysis demonstrate that the sulfurized CFTS and CCdTS-based CEs are more efficient for tri-iodide reduction as compared to the N_2-annealed CFTS and CCdTS-based CEs. The photoconversion efficiencies (PCEs) of DSSCs fabricated with sulfurized, annealed in N_2 atmosphere CFTS and CCdTS as CEs are found to 7.36 ± 0.00%, 5.78 ± 0.12% and 7.12 ± 0.08%, 5.30 ± 0.00% respectively, while the DSSCs fabricated with conventional Pt-based CEs show an efficiency of 8.15 ± 0.09%. These results indicate that the annealing atmosphere of the CEs has an impact on the DSSCs performance.

Received 31st December 2016
Accepted 17th February 2017

DOI: 10.1039/c6ra28889h

rsc.li/rsc-advances

1. Introduction

Solar energy is a renewable energy source that can meet the global energy demands in future and can emerge as an alternative to the traditional non-renewable fossil resources.[1,2] Dye-sensitized solar cells (DSSCs) are promising alternative photovoltaic devices, owing to their low fabrication cost, reasonable photoconversion efficiency (PCE) and ability to work under low light conditions as compared to other solar cells (thin film solar cells, silicon solar cells).[1–4] Recently, considerable efforts have been made in the direction of optimization of DSSCs components (photoanode, electrolyte and counter electrode (CE)), to enhance the performance of the device.[2–8] The CE plays an important role in the performance of DSSCs.[2,5] The electrochemical catalytic activity of CEs determines the rate of conversion of I_3^-/I^-, which also helps in the regeneration of the dye.[2,5] The most commonly used CE in DSSCs is Pt due to its high conductivity and superior electrochemical catalytic activity.[2] However, the scarcity of Pt and its high cost restrict the large-scale commercial application of DSSCs.[2]

Numerous materials such as carbon, conducting polymers, alloys, and inorganic materials have been used as a substitute for Pt-CE.[2,6–12] Among the inorganic materials, earth-abundant quaternary chalcogenides such as Cu_2FeSnS_4 (CFTS), Cu_2CoSnS_4 (CCoTS), Cu_2CdSnS_4 (CCdTS), $Cu_2ZnSnSe_4$ (CZTSe), and Cu_2ZnSnS_4 (CZTS) have shown similar electrochemical catalytic activity to Pt and have been explored as a CE materials in DSSCs.[12–18] Previously, a solvothermally prepared CCdTS based CE for DSSCs demonstrated a PCE of 4%.[16] Spray pyrolysis and solvothermally prepared CFTS based CEs for DSSCs have shown efficiencies of 8% and, 7.1% respectively.[12,18] However, the effect of the sulfurization on the electrical and electrochemical catalytic activities of CFTS and CCdTS films and its impact on DSSCs performance has not yet been reported.

CCdTS and CFTS nanoparticles have been synthesized by various techniques such as high-temperature solid-state reaction processes,[19,20] solvothermal processes,[12,16] spray pyrolysis,[18,21] RF magnetron sputtering,[22] hot injection,[17,23,24] *etc.* However, the synthesis of nanocrystalline, earth-abundant quaternary chalcogenides with precise control over stoichiometry is still a challenge for research groups. Among all the synthesis processes, the thermal decomposition process has

Department of Metallurgical Engineering & Materials Science, Indian Institute of Technology Bombay, Mumbai-400076, India. E-mail: krishrama33@gmail.com; mallick@iitb.ac.in; Fax: +91 2225726975; Tel: +91 2225767641

† Electronic supplementary information (ESI) available. See DOI: 10.1039/c6ra28889h

been reported as a simple route for the synthesis of quaternary chalcogenides at low temperature in a short time (1 h) to obtain crystalline nanoparticles.[14,25]

In this study, we report the synthesis of CCdTS and CFTS nanoparticles by the thermal decomposition process, which requires low temperature (300 °C) and short processing time (1 h) to get crystalline nanoparticles. The effects of the annealing atmosphere on the electrical and electrochemical catalytic activities of the prepared films are studied. Sulfurized CFTS and CCdTS films show better electrocatalytic activity as compared to N_2 annealed CFTS and CCdTS films. DSSCs fabricated with sulfurized CEs demonstrate a higher PCE as compared to CEs based on films annealed in N_2 atmosphere.

2. Experimental details

2.1 Synthesis of quaternary chalcogenide nanomaterials and fabrication of the counter electrodes

The experimental procedure for the synthesis of nanomaterials *via* the thermal decomposition process has been reported elsewhere.[14] The raw materials used in the synthesis of chalcogenide nanomaterials are given in the ESI.† In brief, the stoichiometric ratios of 2 : 1 : 1 : 4: for Cu : Fe : Sn : S of precursor salts were taken in a polypropylene (PP) bottle along with ethanol and zirconia grinding media. The precursor mix was then transferred to a crucible, which was kept in a tubular furnace. The synthesis was carried out at different temperatures, ranging from 300 °C to 500 °C for 1 h in N_2 atmosphere to study the phase formation of CFTS nanoparticles. Cadmium dihydrate was used as a Cd source instead of iron(III) nitrate nonahydrate; the same experimental procedure (as for CFTS) was repeated, for the synthesis of CCdTS nanoparticles. The nanoparticles, prepared at 350 °C for 1 h, were dispersed in organic solvent (hexanethiol) to make stable inks. The prepared stable CFTS/CCdTS inks were coated on soda lime glass (SLG) and fluorine-doped tin oxide (FTO, TEC 8, Pilkington) substrates in a fume hood by using the doctor blade technique for the formation of the films. The prepared films were annealed in N_2 atmosphere and sulfurized (sulfurization process was carried out in the presence of sulfur powder (100 mg) in an inert (N_2) atmosphere) at 525 °C for 30 min. For convenience, sulfurized CFTS and CCdTS films are denoted as S–CFTS and S–CCdTS, and films annealed in N_2 atmosphere are represented as N–CFTS and N–CCdTS.

2.2 Assembly of DSSCs

The detailed fabrication steps for the photoanode (TiO_2), the electrolyte composition used for DSSCs and their assembly are reported in the ESI.† DSSCs were fabricated using the dye-sensitized TiO_2 films as photoanodes and S–CCdTS, S–CFTS, N–CFTS and N–CCdTS based CEs were prepared, respectively. Surlyn spacer (60 μm) was sandwiched between the electrodes, which maintained a constant spacing between them. The electrolyte was injected into the gap between the electrodes. For comparative studies, DSSCs were also fabricated with sputtered Pt-based CEs.

2.3 Characterization

The crystallinity of the as-prepared CCdTS and CFTS nanoparticles and annealed films were characterized by using X-ray diffraction (XRD) (PANalytical X-ray diffractometer) and Raman spectroscopy (HORIBA, HR800). The particle sizes and shapes of the synthesized nanoparticles were examined by a field emission gun transmission electron microscope (FEG-TEM, JEM-7210F). The morphologies of fabricated CCdTS and CFTS films were analyzed using a field emission gun-scanning electron microscope (FEG-SEM, JSM-7600F). Elemental analysis of synthesized nanoparticles and annealed films was conducted using energy dispersive spectroscopy (EDS) attached to a FEG-SEM. Electrical properties of the CCdTS and CFTS films coated on soda lime glass (SLG) substrate were estimated by using Hall effect measurements in a magnetic field strength of 0.67 T at room temperature (Lake Shore, Model 8404 AC/DC). Silver paste was applied at the corner of square shaped CCdTS and CFTS films (7 mm × 7 mm) for making electrical contact for Hall measurements. Electrocatalytic activities of prepared films were studied using cyclic voltammetry. Cyclic voltammetry measurements were carried out using a three-electrode system in an iodide/triiodide electrolyte solution at a scan rate of 50 mV s^{-1} (in the potential range from −1 to 1.8 V). The electrolyte was comprised of 0.1 M LiI, 0.05 M I_2, 1 M $LiClO_4$ and acetonitrile. Pt wire was used as the CE, Ag/AgCl was used as the reference electrode and the prepared S–CFTS, S–CCdTS, N–CCdTS and N–CFTS films were used as the working electrodes. Current density–voltage (*J–V*) characteristics of fabricated DSSCs were recorded using a Keithley 2420 source meter (Keithley Instruments, Inc.) under illumination (90 mW cm^2). The incident photon to current efficiency (IPCE) of DSSCs was measured in the wavelength range from 300–800 nm using a xenon lamp (Bentham PVE300). Electrochemical impedance spectroscopy (EIS) of the symmetric cells of the CEs were measured over a frequency range from 1 MHz to 0.1 Hz with an amplitude of 10 mV by using PGSTAT (AUTOLAB 302N). Tafel polarization of the symmetric cell was performed at a scan rate of 50 mV s^{-1} to verify the electrocatalytic activity of the CE through its exchange current density.

3. Results and discussion

XRD patterns of CFTS and CCdTS nanoparticles synthesized at different temperatures ranging from 300 °C to 500 °C for 1 h are shown in Fig. 1a and b. All the diffraction peaks in Fig. 1a and b are in good agreement with their standard crystal structure patterns for CFTS (JCPDS no. 44-1476) and CCdTS for (JCPDS no. 26-0506), respectively. The average crystallite sizes of CFTS and CCdTS nanoparticles prepared at different temperatures for 1 h were calculated by using the Scherrer formula.

The obtained crystallite sizes of the synthesized nanoparticles are summarized in Table S1 in ESI.† The crystallite size of CCdTS nanoparticles increased from 6 nm to 23 nm with the increase in the temperature from 300 °C to 500 °C. Similarly, the increase in the crystallite size of CFTS nanoparticles was observed with the increase in the temperature. The XRD patterns of prepared films

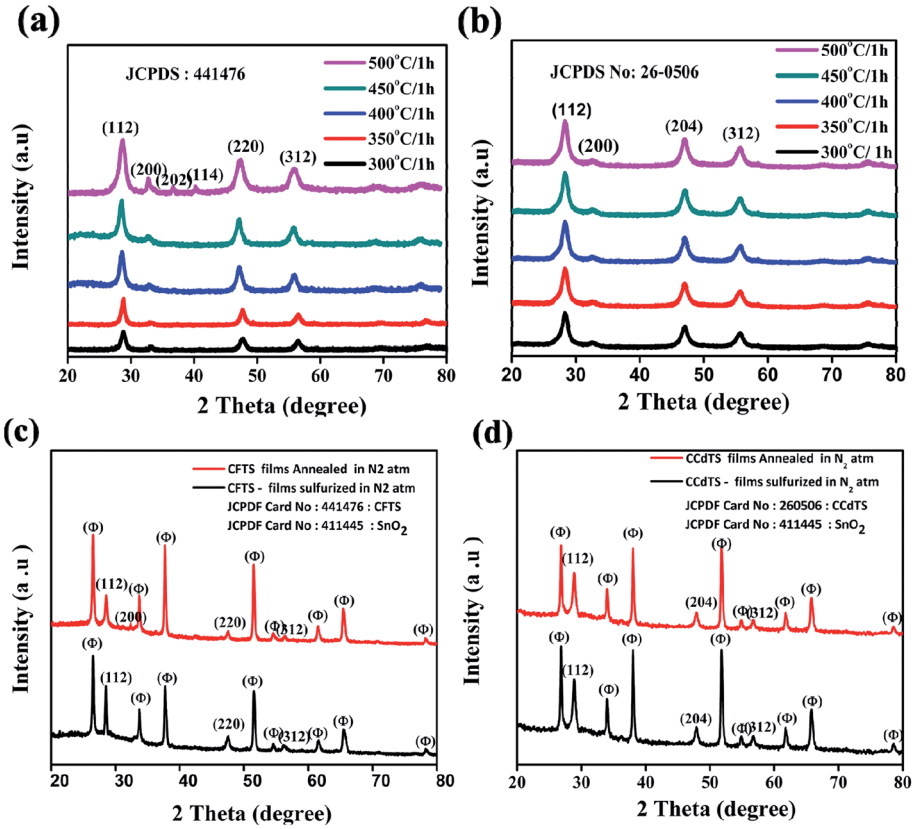

Fig. 1 XRD patterns of (a) CFTS and (b) CCdTS nanoparticles prepared at different temperatures for 1 h. (c) CFTS film coated FTO substrate. (d) CCdTS film coated FTO substrate annealed at 525 °C for 30 min in a different atmosphere (atm).

show additional peaks (θ) along with main phases, which are attributed to the FTO substrate (SnO_2: JCPDS no. 411445, Fig. 1c and d). However, XRD characterization is insufficient to distinguish the crystal structure of CCdTS and CFTS from their secondary phases (Cu_2SnS_3, CdS, and FeS), due to their similar XRD patterns. Raman spectroscopy measurements were performed to further confirm the single phase formation of the as-prepared nanoparticles and annealed films.

Raman spectra of the prepared nanoparticles (300 °C for 1 h) and annealed films are shown in Fig. 2. The peak at 317 cm^{-1} belongs to the CFTS crystal structure (Fig. 2a) and the peaks at 329 cm^{-1} and 281 cm^{-1} correspond to the CCdTS phase (Fig. 2b). The peaks at 317 cm^{-1} and 329 cm^{-1} are attributed to the symmetric vibrational motion of the sulfur atoms in CFTS and CCdTS, respectively.[16,19,20,23,26] The peak at 281 cm^{-1} is ascribed to the vibrations of the Cd atoms and S atoms with some contribution from the Cu atoms in the CCdTS lattice.[19,20,26] The absence of peaks at 293 cm^{-1} (FeS), 318 cm^{-1} (Cu_2SnS_3) and 305 cm^{-1} (CdS) shows the formation of single phase CCdTS and CFTS synthesized nanoparticles and their respective annealed

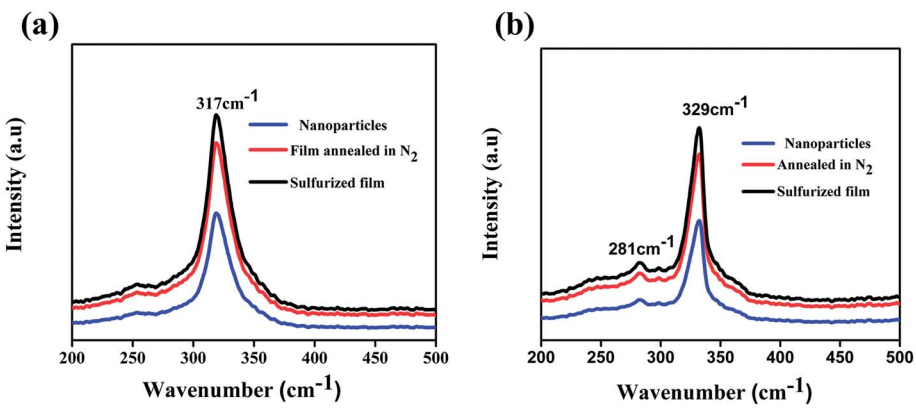

Fig. 2 Raman spectra of (a) CFTS, (b) CCdTS nanoparticles synthesized at 300 °C for 1 h and films annealed at 525 °C for 30 min respectively.

films.[19,20,23,26,27] The obtained values are in good agreement with the literature reported values.[19,20,26]

Bright field FEG-TEM images of CCdTS and CFTS nanoparticles synthesized at 300 °C for 1 h are shown in Fig. 3. Synthesized CCdTS nanoparticles are spherical in shape and have a size of approximately 6–9 nm (Fig. 3a and b). The synthesized CFTS nanoparticles are equiaxed, with sizes of approximately 8–12 nm (Fig. 3e and f). The morphologies of CFTS and CCdTS nanoparticles prepared by thermal decomposition are similar to the nanoparticles synthesized by using wet chemical processes.[12,16,17,23,24] HR-TEM images of CCdTS and CFTS nanoparticles show the clear lattice planes, which indicate the crystallinity of synthesized nanoparticles (Fig. 3c and g, respectively). The selected area electron diffraction (SAED) confirms the polycrystalline nature of synthesized CCdTS and CFTS nanoparticles (Fig. 3d and h). Diffraction rings are indexed to the (112), (204) and (312) planes, which correspond to the stannite CCdTS crystal structure (Fig. 3d). Similarly, (112), (220) and (312) planes (Fig. 3h) are matched to the stannite CFTS crystal structure. The XRD, Raman, and FEG-TEM analysis confirm the crystallinity of CCdTS and CFTS nanoparticles prepared at 300 °C for 1 h.

The average elemental compositions (atomic weight%) of synthesized CFTS and CCdTS nanoparticles and films annealed in different atmospheres were measured by using EDS. The obtained results are shown in Fig. 4 (also see the raw data in Tables S2–S5†). Fe-rich, Sn-rich, and S-deficient CFTS nanoparticles were obtained *via* low-temperature synthesis, while Cd-rich, Sn-rich, and S-deficient CCdTS nanoparticles were obtained (Fig. 4a and b). Excess Cu, Sn-deficiency and the appropriate ratio of Fe and S were noticed for CFTS nanoparticles, while Cu-rich, Sn-deficiency, and the desired ratio of Cd and S were obtained for CCdTS nanoparticles synthesized at high temperature. Similarly, Cu-rich, and Sn and S-deficiencies were observed in both films (N–CCdTS and N–CFTS) annealed in the N_2 atmosphere, while the desired stoichiometric ratio was observed for sulfurized films (Fig. 4c and d). The deficiencies of Sn and S in both films (N–CCdTS, N–CFTS) annealed in N_2 atmosphere are due to the evaporation of Sn and S from the film at high temperature.[28,29]

Surface features of films annealed in N_2 atmosphere and sulfurized film are shown in Fig. 5. The larger grain sizes are observed in N–CCdTS and N–CFTS films (Fig. 5a and b), compared to the S–CCdTS, S–CFTS films (Fig. 5c and d). The larger grain sizes in films annealed under nitrogen might be due to the Cu-rich phase, which is consistent with a previous report.[30]

The electrical properties of all CCdTS and CFTS films were evaluated by using Hall measurements and are given in Table 1. Hall measurements confirm the P-type conductivity of CFTS and CCdTS films. The resistivities of sulfurized CFTS and CCdTS films are smaller than those of the films annealed in N_2 atmosphere. The mobility of sulfurized films is higher than that of the films annealed in N_2 atm. The higher resistivity, the lower mobility of CCdTS film is due to changes in morphology and deviation in the stoichiometric ratio of CFTS films.[12,31] The deficiency of S and Sn creates elementary defects (sulfur vacancy (V_S) and tin vacancy (V_{Sn})) in the prepared films, which can trap electrons, thus increasing the resistivity of the films.[31,32] The obtained electrical properties of CCdTS and CFTS films are similar to the reported values.[12,18,33]

It is essential to evaluate the electrochemical catalytic activity of synthesized materials for their substitution as alternative electrocatalyst materials for CEs in DSSCs. Cyclic voltammetry measurements of prepared films show two pairs of redox peaks (Fig. 6a), which indicate that synthesized materials can act as electrocatalysts for the reduction of I_3^- to I^-. The redox pair at a lower potential is ascribed to the reaction of I_3^-/I^-, which is responsible for the regeneration of the dye in DSSCs.[12] However, the redox pair at higher potential corresponds to the reaction of I_2/I_3^- (Fig. 6a). The electrochemical catalytic parameters such as cathodic current density (I_{pc1}) and peak-to-peak separation (E_{pp})

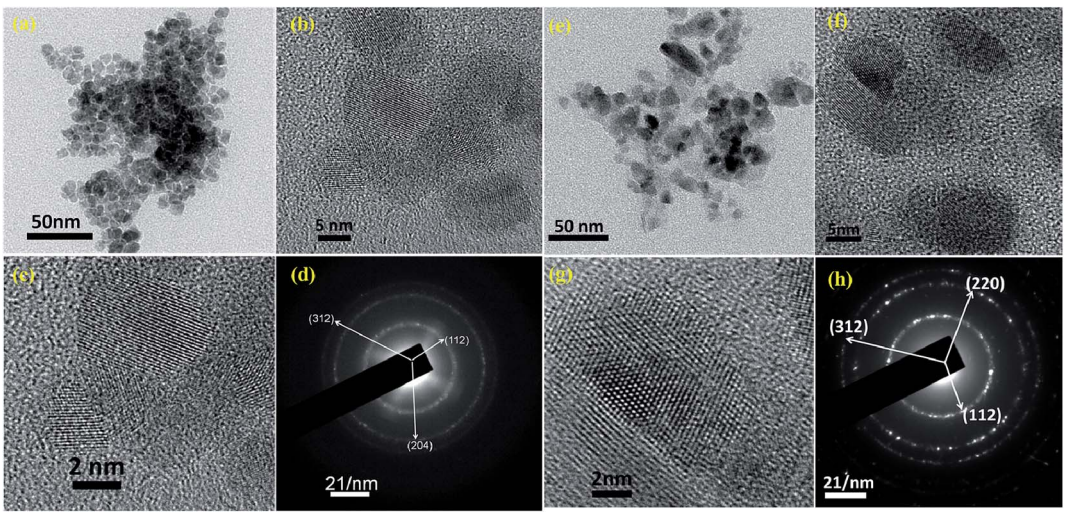

Fig. 3 (a), (b) and (c) FEG-TEM and HRTEM images of CCdTS nanoparticles; (e), (f) and (g) FEG-TEM and HRTEM images of CFTS nanoparticles; (d) and (h) selected-area electron diffraction (SAED) patterns of CCdTS and CFTS nanoparticles, respectively.

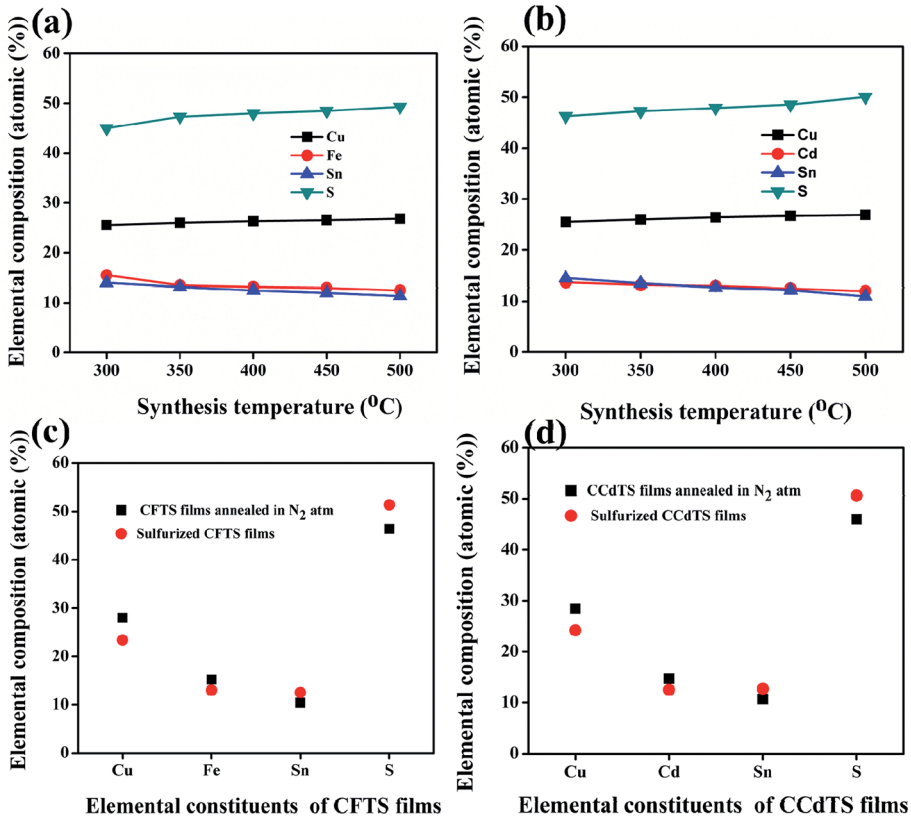

Fig. 4 Elemental compositions of (a) CFTS and (b) CCdTS nanoparticles synthesized at different temperatures (300 °C to 500 °C) for 1 h in N_2 atm. (c) and (d) Elemental compositions of CFTS and CCdTS films annealed in different atmospheres at 525 °C for 30 min.

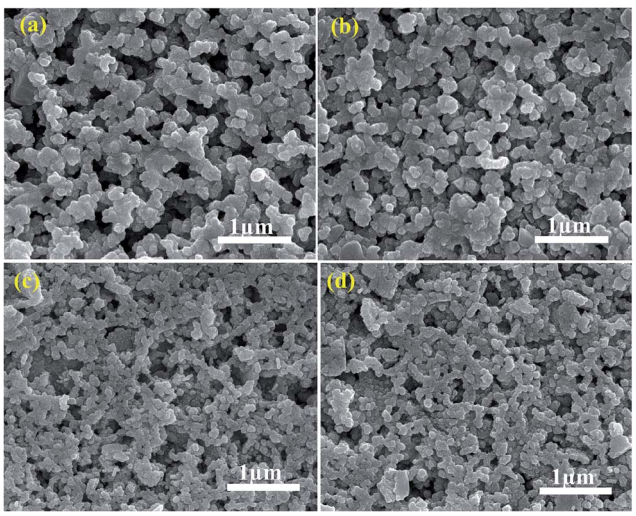

Fig. 5 FEG-SEM images of the top surfaces of CCdTS and CFTS: (a) CFTS film and (b) CCdTS film annealed at 525 °C for 30 min in N_2 atmosphere; (c) CFTS film and (d) CCdTS film sulfurized at 525 °C for 30 min.

of the redox pair at lower potentials are the key parameters for determining the electrocatalytic activity of prepared CEs.[12,18] The electrochemical catalytic parameters (I_{pc1}, E_{pp}) of different CEs obtained from the cyclic voltammogram (CV) curves are given in Table 2 (Fig. 6a). From the CV analysis, the higher I_{pc1} values and lower E_{pp} values of S–CFCTS-CE and S–CFTS-CE indicate a better electrocatalytic activity for the reduction of I_3^- ions in the electrolyte solution, compared to N–CFTS-CE and N–CCdTS-CE, but inferior activity to that of Pt-CE. According to the literature, the elemental compositions,[12,31,34] morphologies,[35,36] electrical conductivities,[12,37–39] crystal structures,[40] secondary phases,[41] and specific surface areas[12,42–44] of CE materials affect the electrochemical catalytic parameters. The higher electrocatalytic activity of S–CFTS-CEs and S–CCdTS-CEs as compared to N–CFTS-CE and N–CCdTS-CE might be due to the variation in elemental composition (Fig. 4c and d), morphology (Fig. 5) and electrical conductivity (Table 1).

Stability assessment of CEs is an important issue for practical application of the DSSCs.[45] According to the reported literature, successive CV scanning, EIS scanning, long-term

Table 1 Electrical properties of CCdTS and CFTS films

Parameters	N–CFTS	N–CCdTS	S–CFTS	S–CCdTS
Type of conductivity	P	P	P	P
Mobility ($cm^2\ V^{-1}\ s^{-1}$)	1.7	1.2	4.5	3.2
Carrier concentration (cm^{-3})	3×10^{17}	2.5×10^{17}	3.3×10^{17}	2.7×10^{17}
Resistivity (Ω cm)	0.56	0.98	2×10^{-2}	7×10^{-2}

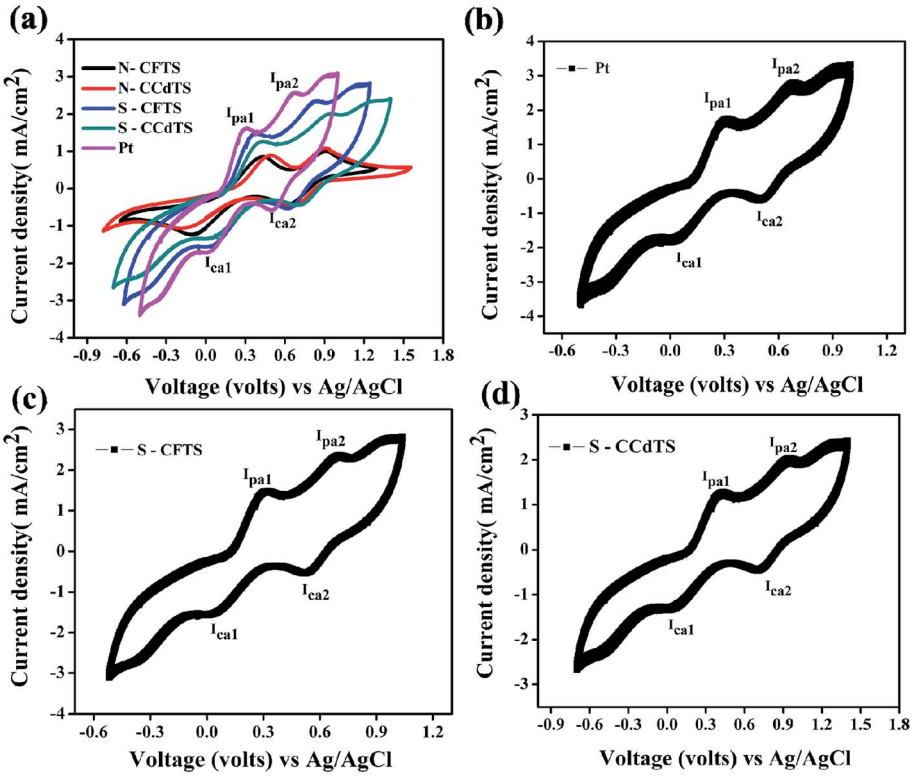

Fig. 6 Cyclic voltammogram curves of (a) different CEs (Pt, N–CCdTS, N–CFTS, S–CCdTS, and S–CFTS) (b) 100 cycles for Pt-CE, (c) 100 cycles for S–CCdTS-CE and (d) 100 cycles for S–CFTS-CE.

stability, dark and illuminated current–voltage testing and the removal rate of the films (mechanical stability) are used to examine the preliminary stability of various CEs.[45–50] Herein, mechanical stability (adhesion of CEs to substrates (FTO)), chemical stability (inert)/dissolution studies and successive CV scanning of CEs are reported for stability assessment of CEs. Adhesion between CE/FTO interfaces influence the performance of DSSCs and the device lifetime.[45] The adhesion test was performed by using an ultrasonicator. The S–CCdTS-CE and S–CFTS-CE were immersed in ethanol and subjected to ultrasonication for 1 h. These CEs were periodically observed after 15 min. As observed from Fig. S1 and S2 (see, ESI†), no major changes were noticed in both the CEs after 1 h. This indicates that the CEs are mechanically stable (well adherent to the FTO substrate). S–CFTS-CE and S–CCdTS-CE were immersed in iodine based electrolyte for 14 days to study the dissolution of prepared CEs (Fig. S3†). These CEs were periodically observed after 7 days. The CEs did not dissolve in electrolyte, even after 14 days, indicating that these CEs are stable (inert) in iodine-based electrolyte (Fig. S4 and S5†). Cyclic voltammetry was carried out for 100 consecutive cycles at 50 mV s^{-1} scan rate to confirm the stability of S–CCdTS-CE and S–CFTS-CE in the iodide based (I_3^-/I^-) electrolyte system. The CV curves of S–CCdTS and S–CFTS-CEs (after 100 cycles) were found to be analogous to that of Pt-CE (Fig. 6b–d). The unchanged shape of the CV curves and nearly constant current density demonstrate the electrochemical stability of the S–CCdTS-CE and S–CFTS-CE in the iodide based electrolyte. The adhesion test, dissolution studies and successive CV scanning of CEs indicate that prepared CEs are quite stable in iodide based electrolyte. However, the aging study of DSSCs fabricated with these CEs (S–CFTS-CE and S–CCdTS-CE) and symmetric cells of CEs under illumination conditions (60 °C, 1 sun) is important for practical application.[45] The aging studies of DSSCs with these CEs are in progress.

Table 2 Electrocatalytic parameters as estimated from the CV curves of prepared CEs

CEs	I_{ca1} (mA cm^{-2})	I_{pa1} (mA cm^{-2})	E_{pp} (meV)	$D \times 10^{-6}$ (cm^2 s^{-1})	$k_0 \times 10^{-4}$ (cm s^{-1})	$\Psi \times 10^{-9}$ (mol cm^{-3})
Pt	1.68	1.61	280	6.2	6.0	2.06
S–CFTS	1.52	1.47	328	5.2	5.5	1.85
S–CCdTS	1.30	1.27	367	3.8	4.7	1.58
N–CFTS	1.25	0.85	527	3.2	4.2	1.50
N–CCdTS	1.09	0.90	638	2.4	3.7	1.24

To further support the electrocatalytic activity of prepared CEs, the adsorption quantity (Ψ) and diffusion coefficient ($D_{I_3^-}$) of I_3^- ions in the electrolyte, and electrochemical rate constant (k_0) of I_3^-/I^- reaction were calculated for the prepared CEs. The Ψ, $D_{I_3^-}$ and k_0 values of I_3^- ions for different CEs were estimated using the following equations,[12,37,39,51] and the obtained results are listed in Table 2.

$$I_{pc1} = [(nF)^2 v\Psi]/RT \quad (1)$$

$$I_{pc1} = Kn^{3/2}A(D_{I_3^-})^{1/2}v^{1/2}C \quad (2)$$

$$\theta = 0.299 \times v^{1/2} \quad (3)$$

$$k_0 = \theta((\Pi DnvF)/RT)^{1/2} \quad (4)$$

where I_{pc1} is the cathodic peak current density (obtained from the CV curves), n is the number of electrons involved in the redox reaction, F is the Faraday constant, R is the universal gas constant, T is the absolute temperature, v is the scan rate, Ψ is the adsorption quantity of the reacting ion (I_3^-), A is the area of CEs, C is the triiodide concentration, θ is a dimensionless kinetic parameter, K is a constant of (2.69×10^5 C mol^{-1} V$^{-1/2}$), Π is a constant (3.14), and k_0 is the electrochemical rate constant of the I_3^-/I^- reaction.

The estimated Ψ value of I_3^- ions for S–CFTS-CE, S–CCdTS-CE was found to be larger than that of N–CFTS-CE, N–CCdTS-CE, but smaller than Pt-CEs. The higher Ψ value for S–CFTS-CE and S–CCdTS-CE shows that larger numbers of I_3^- ions are adsorbed on the S–CFTS and S–CCdTS surfaces as compared to N–CFTS-CE and N–CCdTS-CE surfaces. The estimated Ψ values of different CE materials show a similar order of magnitude to other materials.[12] The calculated diffusion coefficients ($D_{I_3^-}$) of I_3^- ions in the electrolyte for S–CFTS-CE, S–CCdTS-CE are higher than N–CFTS-CE, N–CCdTS-CE, which is ascribed to the slower diffusion of I_3^- ions towards the CEs surface.[12,36–38] The variation in the $D_{I_3^-}$ of I_3^- ions for different CEs is due to the change in electrical conductivity of the CEs.[12,36–38] The estimated k_0 values of S–CFTS-CE and S–CCdTS-CE are greater than that of N–CFTS-CE and N–CCdTS-CE. The larger k_0 value of sulfurized CEs indicates the faster rate of reduction of I_3^- to I^- ions at the CE/electrolyte interface.[19] According to the existing literature, the k_0 value is inversely proportional to the E_{pp} value, and calculated k_0 values are in good accordance with E_{pp} values of different CEs obtained from CV curves (Fig. 6). The larger Ψ, $D_{I_3^-}$, and k_0 values for S–CFTS-CE and S–CCdTS-CE further confirm the more efficient reduction of I_3^- to I^-, compared to N–CFTS-CE and N–CCdTS-CE.

Electrocatalytic activity of CEs was further confirmed by EIS and Tafel polarization measurements. EIS and Tafel polarization measurements of symmetric cells of CEs were performed under illumination at zero bias voltage and the obtained spectra are shown in Fig. 7. The equivalent circuits of the EIS spectra were fitted with the Zsimp software (inset Fig. 7a). Electrochemical parameters such as exchange current density (J_0) (obtained from Tafel polarization, Fig. 7b), series resistance (R_s), charge-transfer resistance (R_{ct}) and the corresponding constant phase angle (CPE) at the electrolyte/CEs interface estimated from the EIS spectra are given in Table 3. The R_{ct} value of different CEs calculated from the EIS spectra and Tafel polarization curves are in good agreement (more details regarding the calculation of R_{ct} and J_0 value from Tafel polarization curves are given in ESI†). According to the previous literature, J_0 and R_{ct} values are correlated with the electrocatalytic activity of CEs, and J_0 is inversely proportional to R_{ct}.[12] The R_{ct} value of S–CFTS-CE (2.9 Ω cm^2) and S–CCdTS-CE (3.8 Ω cm^2) are found to be smaller than those of N–CFTS-CE (5.0 Ω cm^2), and N–CCdTS-CE (6.9 Ω cm^2), respectively. The obtained R_{ct}, and J_0 values indicate that sulfurized CEs are more

Table 3 Electrochemical parameters obtained from EIS and Tafel polarization for different CEs

CE	Pt	S–CFTS	S–CCdTS	N–CFTS	N–CCdTS
R_s (Ω cm^2)^a	10.9	11.37	12.30	13.2	12.4
R_{ct} (Ω cm^2)^a	2.1	2.9	3.8	5.0	6.9
CPE (μF)^a	42	38	39	34	32
R_{ct} (Ω cm^2)^b	2.4	3.3	4.1	5.4	7.1
J_0 (mA cm^{-2})^b	4.8	3.7	3.1	2.3	1.8

^{a} Calculated from EIS spectra. ^{b} Calculated from Tafel polarization.

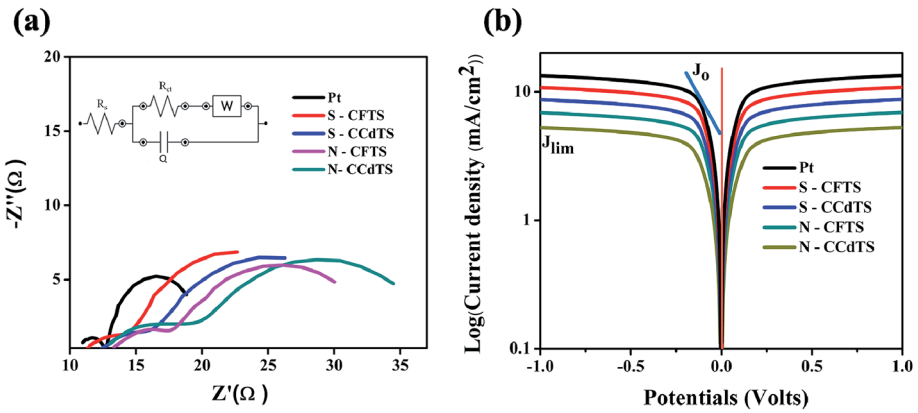

Fig. 7 (a) EIS spectra and (b) Tafel plots of symmetric cells fabricated with two identical CEs.

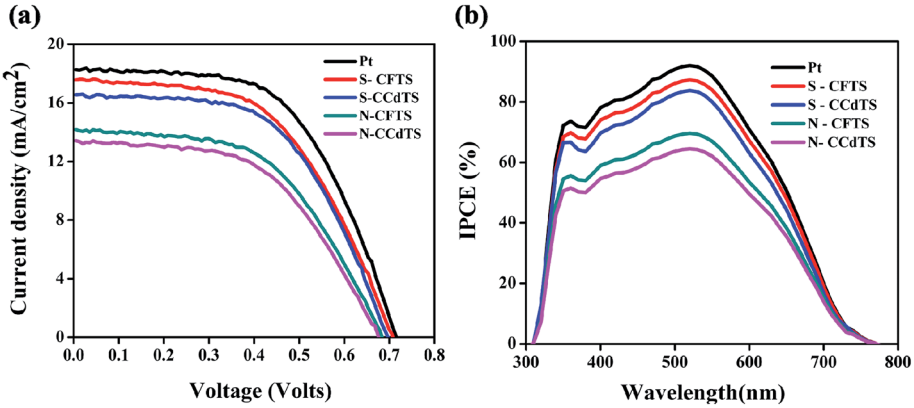

Fig. 8 (a) J–V curves and (b) IPCE spectra of fabricated DSSCs with different CEs.

efficient for the reduction of I_3^- to I^- at the electrolyte–CE interface, as compared to the N_2 annealed CEs; however, it is less efficient in comparison to Pt CEs. The variation in R_s value for different CEs might be due to the change in their electrical resistivity and adhesion of the films to the FTO substrate.[12,36–38] From the CV, EIS and Tafel analysis indicate that sulfurized CEs possess better electrochemical activity, compared to the N_2 annealed CEs.

Current density–voltage (J–V) characteristics of DSSCs assembled with all CCdTS, CFTS, and Pt-based CEs are shown in Fig. 8a. Average (five cells) solar cell parameters such as short-circuit current density (J_{sc}), open circuit voltage (V_{oc}), fill factor (FF), and efficiency (η) estimated from the J–V characteristics are given in Table 4. The DSSC fabricated with S–CFTS-CE, S–CCdTS-CE showed higher J_{sc}, and V_{oc}, as compared to N–CFTS-CE, N–CCdTS-CE, but lower than that of Pt-based CE.

The lower J_{sc} of N–CFTS-CE, N–CCdTS-CE could be ascribed to higher resistivity and lower electrochemical catalytic activity.[12,31] The open circuit voltages of DSSCs fabricated from S–CFTS-CE and S–CCdTS-CE are higher than that from N–CFTS-CE and N–CCdTS-CE. The variation in V_{oc} of DSSCs fabricated with different CEs is explained with the help of the following equation:[17,52]

$$V_{oc} = (k_B T/e) \times \ln(I_{inj}/[n_{cb} k_{et} C]) \quad (5)$$

where V_{oc} is the open circuit voltage, k_B is the Boltzmann constant, T is the absolute temperature, e is an electronic charge, I_{inj} is the flux of charge resulting from sensitized injection, n_{cb} is the electron concentration on the surface of TiO_2, k_{et} is the reaction rate constant of the I_3^- dark reaction on TiO_2, and C is the triiodide concentration in electrolyte.

The change in V_{oc} of different CEs might be due to the presence of a high concentration of I_3^- ions in the electrolyte, which is ascribed to the slower rate of conversion of I_3^-/I^- at the CE surface–electrolyte interface.[8] The calculated J_{sc}, V_{oc} of DSSCs fabricated with different CEs are in accordance with the electrical conductivity and electrochemical parameters of different CEs estimated from CV analysis. DSSCs fabricated with S–CFTS-CE, S–CCdTS-CE, and N–CFTS-CE, N–CCdTS-CE demonstrated an efficiency of 7.36 ± 0.00%, 7.12 ± 0.08% and 5.78 ± 0.12%, 5.30 ± 0.00%, respectively, while the one fabricated with Pt-CE exhibited an efficiency of 8.15 ± 0.09%. The lower fill factor of DSSCs with N–CCdTS-CE and N–CFTS-CE is due to a higher R_s value (Table 3). The measured IPCE spectra of DSSCs fabricated with prepared CEs are shown in Fig. 8b. IPCE response at 350 nm is ascribed to the direct band gap photoelectron excitation of TiO_2.[12] The IPCE of DSSCs with S–CFTS-CE, S–CCdTS-CE, N–CFTS-CE, N–CCdTS-CE are observed to be about 87.3%, 83.5%, 69.8%, 63.8% at 520 nm, respectively, while IPCE of DSSCs with Pt-CE is found to be 92.8% at 520 nm. The IPCE spectra results are in good agreement with the J_{sc} value of DSSCs fabricated with prepared CEs.

Table 4 Average (five cells) solar cell parameters of DSSCs fabricated with different CEs

CEs	J_{sc} (mA cm^{-2})	V_{oc} (mV)	FF	η (%)
Pt	18.27 ± 0.31	713.6 ± 1.28	0.60 ± 0.00	8.15 ± 0.09
S–CFTS	17.37 ± 0.32	705.2 ± 0.96	0.57 ± 0.00	7.36 ± 0.00
S–CCdTS	16.38 ± 0.25	695.6 ± 1.44	0.56 ± 0.00	7.12 ± 0.08
N–CFTS	14.59 ± 0.37	684.6 ± 1.68	0.54 ± 0.00	5.78 ± 0.12
N–CCdTS	13.29 ± 0.27	675.0 ± 2.08	0.53 ± 0.00	5.30 ± 0.00

4. Conclusions

Quaternary chalcogenides (Cu_2FeSnS_4 (CFTS) and Cu_2CdSnS_4 (CCdTS) nanoparticles) have been synthesized by the thermal decomposition of metal precursors at different temperatures (300 °C to 500 °C) for 1 h. XRD, Raman spectroscopy, and FEG-TEM analysis revealed that heat treatment at 300 °C for 1 h is enough to form single phase CFTS and CCdTS nanoparticles. Sn and S-deficiencies in N–CCdTS and N–CFTS films led to higher resistivity as compared to S–CFTS and S–CCdTS films. Electrical conductivity and electrochemical parameters together demonstrated that S–CFTS-CE and S–CCdTS-CE are more efficient for the rate of conversion of I_3^- to I^-, as compared to N–CFTS-CE and N–CCdTS-CE. The DSSCs fabricated with S–CFTS-CE and S–CCdTS-CE achieved 90% and 87% of the photoconversion efficiency of DSSCs with conventional Pt CE, respectively. The

obtained results indicate that the annealing atmosphere plays a vital role in the performance of DSSCs.

Acknowledgements

Authors would like to thanks to Prof. Parag Bhargava for his assistance regarding the stability of counter electrodes. Authors also extended thanks to SERIIUS and IITB for financial support and SAIF, CEN for analytical analysis supporting the present work.

References

1 M. Ye, X. Wen, M. Wang, J. Iocozzia, N. Zhang, C. Lin and Z. Lin, *Mater. Today*, 2015, **18**, 155–162.
2 L. Wang, M. A. Mamun, P. Liu, Y. Wang, H. G. Yang, H. F. Wang and H. Zhao, *NPG Asia Mater.*, 2015, **7**, 1–15.
3 S. Mathew, A. Yella, P. Gao, R. H. Baker, B. F. E. Curchod, N. A. Astani, I. Tavernelli, U. Rothlisberger, M. K. Nazeeruddin and M. Gratzel, *Nat. Chem.*, 2014, **6**, 242–247.
4 A. Fakharuddin, R. Jose, T. M. Brown, F. Fabregat-Santiago and J. Bisquert, *Energy Environ. Sci.*, 2014, **7**, 3952–3981.
5 X. Liu, J. Fang, Y. Liu and T. Lin, *Front. Mater. Sci.*, 2016, **10**(3), 225–237.
6 J. Theerthagiri, A. R. Senthil, J. Madhavan and T. Maiyalagan, *ChemElectroChem*, 2015, **2**, 928–945.
7 Q. Tang, J. Duan, Y. Duan, B. He and L. Yu, *Electrochim. Acta*, 2015, **178**, 886–899.
8 M. Kouhnavard, N. A. Ludin, B. V. Ghaffari, K. Sopian and S. Ikeda, *ChemSusChem*, 2015, **8**, 1510–1533.
9 C. R. Ke, C. C. Chang and J. M. Ting, *J. Power Sources*, 2015, **284**, 489–496.
10 J. Liu, Q. Tang, B. He and L. Yu, *J. Power Sources*, 2015, **282**, 79–86.
11 S. Yun, A. Hagfeldt and T. Ma, *Adv. Mater.*, 2014, **26**, 6210–6237.
12 K. Mokurala, S. Mallick and P. Bhargava, *J. Power Sources*, 2016, **305**, 134–143.
13 S. J. Yuan, Z. J. Zhou, Z. L. Hou, W. H. Zhou, R. Y. Yao, Y. Zhao and S. X. Wu, *Chem.–Eur. J.*, 2013, **9**, 10107–10110.
14 K. Mokurala, A. Kamble, A. Gupta, P. Bhargava and S. Mallick, *Adv. Sci. Lett.*, 2016, **22**, 1026–1028.
15 K. Mokurala, A. Kamble, C. Bathina, P. Bhargava and S. Mallick, *Mater. Today*, 2016, **3**, 1778–1784.
16 K. Mokurala, P. Bhargava and S. Mallick, *IEEE 40th photovoltaic specialist conference (PVSC)*, 2014, vol. 1, pp. 1534–1537.
17 J. Y. Park, J. H. Noh, T. N. Mandal, S. H. Im, Y. Jun and S. Seok, *RSC Adv.*, 2013, **3**, 24918–24921.
18 R. R. Prabhakar, N. H. Loc, M. H. Kumar, P. P. Boix, S. Juan, R. A. John, S. K. Batabyal and L. H. Wong, *ACS Appl. Mater. Interfaces*, 2014, **6**, 17661–17667.
19 C. Rincón, M. Quintero, E. Moreno, Ch. Power, E. Quintero, J. A. Henao, M. A. Macías, G. E. Delgado, R. Tovar and M. Morocoima, *Solid State Commun.*, 2011, **151**, 947–951.
20 K. Timmo, M. K. Kuusik, M. Altosaar, J. Raudoja, T. Raadik, M. Grossberg, T. Varema, M. Pilvet, I. Leinemann, O. Volobujeva and M. Eellikov, *28th European photovoltaic solar energy conference and Exhibition (EU PVSEC 2013)*, 2013, pp. 2385 – 2388.
21 L. Nie, S. Liu, Y. Chai and R. Yuan, *J. Anal. Appl. Pyrolysis*, 2015, **112**, 363–368.
22 X. Meng, H. Deng, J. Tao, H. Cao, X. Li, L. Sun, P. Yang and J. Chu, *J. Alloys Compd.*, 2016, **680**, 446–451.
23 B. Zhou, X. Yan, P. Li, L. Yang and D. Yu, *Eur. J. Inorg. Chem.*, 2015, **1**, 2690–2694.
24 K. Ramasamy, X. Zhang, R. D. Bennett and A. Gupta, *RSC Adv.*, 2013, **3**, 1186–1193.
25 K. Mokurala, P. Bhargava and S. Mallick, *RSC Adv.*, 2015, **5**, 96928–96933.
26 M. Himmrich and H. Haeuseler, *Spectrochim. Acta, Part A*, 1991, **47**, 933–942.
27 K. K. Nanda, S. N. Sarangi, S. N. Sahu, S. K. Deb and S. N. Behera, *Phys. B*, 1999, **262**, 31–39.
28 A. Redinger, D. M. Berg, P. J. Dale and S. Siebentritt, *J. Am. Chem. Soc.*, 2011, **133**, 3320–3323.
29 A. Weber, R. Mainz and H. W. Schock, *J. Appl. Phys.*, 2010, **107**, 013516.
30 T. Tanaka, A. Yoshida, D. Saiki, K. Saito, Q. Guo, M. Nishio and T. Yamaguchi, *Thin Solid Films*, 2010, **518**, S29–S33.
31 M. S. Fan, J. H. Chen, C. T. Li, K. W. Cheng and K. C. Ho, *J. Mater. Chem. A*, 2015, **3**, 562–569.
32 M. Kumar, A. Dubey, N. Adhikari, S. Venkatesan and Q. Qiao, *Energy Environ. Sci.*, 2015, **8**, 3134–3159.
33 K. Tto and T. NakaJawa, *Jpn. J. Appl. Phys.*, 1988, **27**, 2094–2097.
34 S. K. Swami, N. Chaturvedi, A. Kumar, N. Chander, V. Dutta, D. K. Kumar, A. Ivaturi, S. Senthilarasu and H. M. Upadhyay, *Phys. Chem. Chem. Phys.*, 2014, **16**, 23993–23999.
35 Z. Tang, J. Wu, M. Zheng, J. Huo and Z. Lan, *Nano Energy*, 2013, **2**, 622–627.
36 H. Yuan, Q. Jiao, S. Zhang, Y. Zhao, Q. Wu and H. Li, *J. Power Sources*, 2016, **325**, 417–426.
37 W. Hou, Y. Xiao, G. Han, D. Fu and R. Wu, *J. Power Sources*, 2016, **322**, 155–162.
38 J. Song, G. R. Li, C. Y. Wu and X. P. Gao, *J. Power Sources*, 2014, **266**, 464–470.
39 B. He, Q. Tang, M. Wang, C. Ma and S. Yuan, *J. Power Sources*, 2014, **256**, 8–13.
40 X. Lin, M. Wu, Y. Wang, A. Hagfeldt and T. Ma, *Chem. Commun.*, 2011, **47**, 11489–11491.
41 R. K. Bhosale, S. A. Agarkar, I. Agrawal, R. A. Naphade and S. Ogale, *RSC Adv.*, 2014, **4**, 21989–21996.
42 M. Wu, X. Lin, Y. Wang, L. Wang, W. Guo, D. Qi, X. Peng, A. Hagfeldt, M. Gratzel and T. Ma, *J. Am. Chem. Soc.*, 2012, **134**, 3419–3428.
43 Y. Xie, C. Zhang, F. Yue, Y. Zhang, Y. Shi and T. Ma, *RSC Adv.*, 2013, **3**, 23264–23268.
44 J. Wu, Z. Tang, Y. Huang, M. Huang, H. Yu and J. Lin, *J. Power Sources*, 2014, **257**, 84–89.
45 S. Yun, P. D. Lund and A. Hinsch, *Energy Environ. Sci.*, 2015, **8**, 3495–3514.

46 F. Gong, H. Wang, X. Xu, G. Zhou and Z. S. Wang, *J. Am. Chem. Soc.*, 2012, **134**, 10953–10958.
47 S. Yun, M. Wu, Y. Wang, J. Shi, X. Lin, A. Hagfeldt and T. Ma, *ChemSusChem*, 2013, **6**, 411–416.
48 S. Yun, H. Pu, J. Chen, A. Hagfeldt and T. Ma, *ChemSusChem*, 2014, **7**, 442–450.
49 S. Yun, H. Zhang, H. Pu, J. Chen, A. Hagfeldt and T. Ma, *Adv. Energy Mater.*, 2013, **3**, 1407.
50 L. Kavan, J. H. Yum and M. Gratzel, *ACS Nano*, 2011, **5**, 165–172.
51 J. E. Park, S. Song and I. S. Shin, *Int. J. Electrochem. Sci.*, 2016, **11**, 5891–5899.
52 J. Xu, M. Li, L. Wu, Y. Sun, L. Zhu, S. Gu, L. Liu, Z. Bai, D. Fang and W. Xu, *J. Power Sources*, 2014, **257**, 230–236.